Physics-informed neural network analysis of laser-driven solitary waves in a carbon slab target

Katsuya Kondo [1,*] Ryutaro Matsui [1,2] and Kenji Imadera [1]
[1] Department of Fundamental Energy Science, Graduate School of Energy Science, Kyoto University, Uji, Kyoto 611-0011, Japan
[2] National Institute for Fusion Science, Toki, Gifu 509-5292, Japan

(Received 15 March 2026; accepted 11 June 2026; published 24 June 2026)

Solitary waves are important phenomena for particle acceleration and energy transport in both astrophysical and laboratory laser plasmas. To investigate their characteristics, we introduce a physics-informed neural network (PINN)-based method to infer the governing partial differential equation that describes solitary waves in one-dimensional particle-in-cell (PIC) simulations. Benchmark tests using numerical solutions of partial differential equations demonstrate that the PINN can successfully infer advection-diffusion, Burgers, and Korteweg–de Vries (KdV) equations with reasonable accuracy. We then apply the PINN to PIC simulation data modeling the irradiation of a femtosecond laser onto a carbon target, in which a laser-driven peak structure propagates as a solitary wave. Both the PINN-predicted data and the solution of the equation with the PINN-inferred coefficients agree well with the original simulation data. The inferred coefficients indicate that the governing equation is a nonlinear KdV-like equation and that the solitary waves are consistent with the theoretical properties of ion acoustic solitons. These results show that the solitary waves in laser-irradiated plasmas behave as KdV solitons, demonstrating that the proposed method is effective for understanding nonlinear plasma waves.

DOI: 10.1103/qxpb-4w5y

I. INTRODUCTION

Solitary waves, which have large amplitudes and exhibit strong nonlinearity, are ubiquitous throughout the universe and play a key role in particle acceleration and energy transport in plasmas. These solitary waves exhibit the characteristics of Bernstein-Greene-Kruskal waves [1], arising from a balance between nonlinear effects and the stabilizing effect of trapped particles. In the magnetosphere of the Earth, solitary waves are observed in the auroral zone [2], the magnetopause [3], the magnetotail [4], and other regions [5]. In the auroral zone, solitary waves accelerate electrons along ambient magnetic field lines to speeds up to 10^4 times their thermal velocity. Solitary waves are also considered to exist on other planets in the solar system, such as Saturn [6] and Venus [7]. Although Venus has little magnetosphere, solitary waves have been observed by spacecraft missions. Theoretical models suggest that they are involved in mass loss resulting from the interaction between the solar wind and Venus's atmosphere [8,9]. Beyond the solar system, solitary waves are predicted to exist in pulsar winds [10]. Although pulsar winds contain positrons in addition to electrons and

*Contact author: kondo.katsuya.72m@st.kyoto-u.ac.jp

ions, solitary waves are still expected to occur in such electron-positron-ion plasmas. Solitary waves also affect the generation of superthermal electrons and positrons.

Solitary waves have also been extensively investigated in laser-produced plasmas, where similar nonlinear mechanisms emerge. Theory and numerical simulations indicate the significance of solitary waves in particle acceleration and laser energy transport. With femtosecond lasers, solitary waves driven by laser-matter interactions can directly accelerate ions to MeV-scale energies [11,12]. With picosecond lasers as well, solitary waves are generated through the collapse of shocks that accelerate particles [13]. Solitary waves are also generated in the boundary layer between laser-ablated solid matter and ambient gas, where they accelerate gas ions to high energies [14].

A well-known theoretical model for solitary waves is the soliton described by the Korteweg–de Vries (KdV) equation. The KdV equation is considered to govern various systems such as shallow water waves [15], oscillations of nonlinear lattices [16], magnetosonic waves [17], and ion acoustic waves [18] in plasmas. Because of its remarkable characteristics—such as integrability, N-soliton solutions [19], and conservation laws [20]—the KdV equation has been extensively studied in both applied mathematics and physics. KdV solitons emerge as the small-amplitude approximation of the fully nonlinear theory [21], and various theoretical analyses have been conducted based on this framework [9,22]. Whether observed solitary waves correspond to KdV solitons is typically judged from the relationship between the wave amplitude and width. However, it is not straightforward to directly verify that complex nonlinear phenomena in astrophysical and laser plasmas are governed by the KdV equation, which complicates the interpretation of observed plasma waves.

A promising method to address this issue is the physics-informed neural network (PINN), a data-driven approach that employs neural networks with embedded physical laws expressed as partial differential equations (PDEs). Incorporating physical information into the neural network model regularizes the learning process and eliminates unphysical solutions [23]. The PINN model can not only perform accurate forward predictions but also solve inverse problems by estimating the unknown coefficients of the governing equation [24]. PINN models have been shown to be applicable to a wide range of physical systems [25]. In particular, for KdV-type systems, internal solitary waves in oceanic environments have been investigated using PINNs for both forward simulation and inverse parameter estimation [26]. In forward problems, it has been theoretically demonstrated that PINNs can reproduce single-soliton solutions when a sufficient number of training points is provided [27]. For more complex dynamics—such as multiple soliton collisions, soliton fission [28], or interactions in coupled nonlinear systems [29]—embedding conservation laws into the PINN loss function has been shown to improve performance and enable the model to handle these challenging dynamics.

Based on the above background, we introduce a PINN-based method to infer the governing PDE that describes solitary waves in one-dimensional particle-in-cell (PIC) simulations. We apply the PINN to PIC simulation data modeling the irradiation of a femtosecond laser onto a carbon target, in which a laser-driven peak structure propagates as a solitary wave and subsequently splits into three distinguishable solitary waves. In this study, by inferring the PDE that governs such simulation data, we quantitatively evaluate whether the observed waves are ion acoustic solitons described by the KdV equation and demonstrate that the proposed method is effective for understanding nonlinear waves inherent to plasmas.

This paper is organized as follows. In Sec. II, we review the theory of ion acoustic solitons and PINN framework. In Sec. III, we verify the efficiency of the PINN through benchmark tests to infer the advection-diffusion, Burgers, and KdV equations. In Sec. IV, we apply the PINN to one-dimensional electromagnetic PIC simulation data in which laser-driven solitary waves emerge. Section V concludes this paper.

II. THEORETICAL MODEL

In this section, we introduce the theoretical model of ion acoustic solitons and the PINN framework. In Sec. II A, to demonstrate the existence of solitary waves in plasmas, we present the theoretical model of ion acoustic solitons. In Sec. II B, we introduce the data-driven PINN method and discuss the resulting equations.

A. Theoretical model of ion acoustic soliton

First, to demonstrate the existence of solitary waves in electrostatic plasmas, we derive the KdV equation, which has an ion acoustic soliton as a solution [18]. We assume a uniform background plasma with electron density n_0 and electron temperature T_e. The ions are assumed to be cold, and their mass and density are denoted by m_i and n_i, respectively. The length is normalized as $\tilde{x} = x/\lambda_{\rm De}$, where $\lambda_{\rm De}$ is the electron Debye length defined by $\lambda_{\rm De} = \sqrt{T_e/(4\pi n_0 e^2)}$. The time is normalized as $\tilde{t} = t\omega_{\rm pi}$. Here, $\omega_{\rm pi}$ denotes the ion plasma frequency, $\omega_{\rm pi} = \sqrt{4\pi n_0 Z e^2/m_i}$, where e denotes the electron charge and Z is the ion charge number. These normalizations lead to the velocity normalization $\tilde{v} = v/c_s$, where $c_s = \sqrt{ZT_e/m_i}$ is the ion acoustic speed. The densities of electrons and ions are normalized by the density at $x \to \infty$, described by n_0 and n_0/Z, respectively; thus, $\tilde{n}_e = n_e/n_0$ for electrons and $\tilde{n}_i = Zn_i/n_0$ for ions. The electrostatic potential ϕ is normalized as $\tilde{\phi} = e\phi/T_e$. With these normalizations, the continuity equation, the equation of motion, the distribution of adiabatic electrons, and the Poisson equation are written as

$$\frac{\partial \tilde{n}_i}{\partial \tilde{t}} + \frac{\partial}{\partial \tilde{x}}(\tilde{n}_i \tilde{v}) = 0, \tag{1}$$

$$\frac{\partial \tilde{v}}{\partial \tilde{t}} + \tilde{v}\frac{\partial \tilde{v}}{\partial \tilde{x}} = -\frac{\partial \tilde{\phi}}{\partial \tilde{x}}, \tag{2}$$

$$\tilde{n}_e = \exp(\tilde{\phi}), \tag{3}$$

$$\frac{\partial^2 \tilde{\phi}}{\partial \tilde{x}^2} = \tilde{n}_e - \tilde{n}_i. \tag{4}$$

The KdV equation is derived by applying the reductive perturbation method to Eqs. (1)–(4). We introduce the expansions

$$\tilde{n}_i = 1 + \epsilon \tilde{n}_{i1} + \epsilon^2 \tilde{n}_{i2} + \cdots , \tag{5}$$

$$\tilde{\phi} = \epsilon \tilde{\phi}_1 + \epsilon^2 \tilde{\phi}_2 + \cdots , \tag{6}$$

$$\tilde{v} = \epsilon \tilde{v}_1 + \epsilon^2 \tilde{v}_2 + \cdots . \tag{7}$$

The dispersion relation is assumed to be third order with respect to k:

$$\omega = c_s k - \frac{c_s \lambda_{\rm De}^2}{2} k^3, \tag{8}$$

where the cubic term represents the leading-order dispersive correction. According to Eq. (8), the scaling between x and t is given by

$$\xi = \epsilon^{1/2}(\tilde{x} - \tilde{t}), \tag{9}$$

$$\tau = \epsilon^{3/2}\tilde{t}, \tag{10}$$

which is known as the Gardner-Morikawa transformation [17]. By applying the expansion given by Eqs. (5)–(7) and the transformation given by Eqs. (9) and (10) to Eqs. (1)–(4), we obtain the equations order by order. From the lowest order in ϵ, the relation among the normalized velocity, density, and potential is given as

$$\tilde{v}_1 = \tilde{n}_{i1} = \tilde{\phi}_1. \tag{11}$$

From the second lowest order in ϵ, the KdV equation

$$\frac{\partial \tilde{n}_{i1}}{\partial \tau} + \tilde{n}_{i1}\frac{\partial \tilde{n}_{i1}}{\partial \xi} + \frac{1}{2}\frac{\partial^3 \tilde{n}_{i1}}{\partial \xi^3} = 0 \tag{12}$$

is obtained. Note that this equation is written in a moving frame with the ion acoustic speed. By applying the inverse transformation of Eqs. (9) and (10) to Eq. (12) and restoring the dimensional variables, the following KdV equation for the total density n_i in the laboratory frame is obtained:

$$\frac{\partial n_i}{\partial t} + \frac{Zc_s}{n_0} n_i \frac{\partial n_i}{\partial x} + \frac{1}{2} c_s \lambda_{\mathrm{De}}^2 \frac{\partial^3 n_i}{\partial x^3} = 0, \tag{13}$$

where the relation $\tilde{n}_i \simeq 1 + \epsilon \tilde{n}_{i1}$ is assumed. Considering a single-soliton solution with a constant drift velocity U in the laboratory frame, the solution of Eq. (13) is obtained as

$$n_i = \frac{n_0}{Z} + \frac{3n_0}{Z}\frac{U - c_s}{c_s}\mathrm{sech}^2\left(\sqrt{\frac{U - c_s}{2c_s}}\frac{x - Ut}{\lambda_{\mathrm{De}}}\right). \tag{14}$$

Here, the amplitude δn_i and the soliton width D are defined as

$$\delta n_i \equiv \frac{3n_0}{Z}\frac{U - c_s}{c_s}, \tag{15}$$

$$D \equiv \lambda_{\mathrm{De}}\sqrt{\frac{2c_s}{U - c_s}}. \tag{16}$$

The solution in Eq. (14) represents the well-known bell-shaped soliton profile.

Equations (14)–(16) indicate that the characteristics of the soliton—namely, its amplitude, width, and velocity—are determined by a single parameter. In other words, once one of these quantities is specified, the other two, as well as the soliton shape, are uniquely determined. Thus, the characteristics of the soliton are fully determined by the coefficients of the governing equation and a single parameter.

B. Physics-informed neural network model for inverse problems

PINN is a data-driven approach that employs neural networks with embedded physical laws expressed as differential equations. For inverse problems, the loss function L consists of three terms: the mean-squared error between the training data and the predicted data L_{data}, the deviation from the governing equation L_{eq}, and the deviation from the boundary conditions L_{bc}.

We assume that the governing equation takes the form

$$\frac{\partial n_i}{\partial t} + a_x^{(r)}\frac{\partial n_i}{\partial x} + a_{xx}^{(r)}\frac{\partial^2 n_i}{\partial x^2} + a_{xxx}^{(r)}\frac{\partial^3 n_i}{\partial x^3} + a_{nx}^{(r)} n_i \frac{\partial n_i}{\partial x} = 0. \tag{17}$$

Here, $a_x^{(r)}$, $a_{xx}^{(r)}$, $a_{xxx}^{(r)}$, and $a_{nx}^{(r)}$ denote the unknown coefficients of the corresponding differential terms in physical units. These coefficients may vanish depending on the type of governing equation. To determine the unknown coefficients, the loss function of the PINN is defined as

$$L = L_{\mathrm{data}} + k_{\mathrm{eq}} L_{\mathrm{eq}} + k_{\mathrm{bc}} L_{\mathrm{bc}}, \tag{18}$$

$$L_{\mathrm{data}} = \frac{1}{N_{\mathrm{data}} n_{\mathrm{max}}^2}\sum (n_{\mathrm{pred}} - n_{\mathrm{true}})^2, \tag{19}$$

$$L_{\mathrm{eq}} = \frac{1}{N_{\mathrm{data}}}\sum\left(\frac{\partial n_{\mathrm{pred}}}{\partial t_s} + a_x \frac{\partial n_{\mathrm{pred}}}{\partial x_s} + a_{xx}\frac{\partial^2 n_{\mathrm{pred}}}{\partial x_s^2} + a_{xxx}\frac{\partial^3 n_{\mathrm{pred}}}{\partial x_s^3} + a_{nx} n_{\mathrm{pred}}\frac{\partial n_{\mathrm{pred}}}{\partial x_s}\right)^2. \tag{20}$$

Here, (x_s, t_s) denote the coordinates measured in the normalized units used in the simulation. a_x, a_{xx}, a_{xxx}, and a_{nx} denote the coefficients expressed in the normalized simulation units. n_{pred} and

n_{true} represent the predicted and true ion densities, respectively, and n_{max} denotes the maximum value of n_{true}. Note that $n_{\mathrm{true}}, n_{\mathrm{pred}}$, and n_{max} are also expressed in normalized simulation units. Normalizing the data by n_{max} is essential for achieving stable and reliable training. Equation (20) is not normalized and is written in the normalized simulation units. The parameters k_{eq} and k_{bc} denote the loss weights that control the contributions of the governing equation residual term and the boundary condition term, respectively. If k_{eq} is too small, the model fails to learn the form of the governing equation, whereas an excessively large k_{eq} prevents the model from accurately reconstructing the dataset. The term L_{bc} takes different forms depending on the boundary conditions. Since the information on the boundary conditions is included in the simulation data, k_{bc} can be set to zero. For inverse problems, the unknown coefficients in the governing equation are inferred by minimizing the loss function L.

Here, we discuss typical cases of the inferred equations that satisfy $L_{\mathrm{eq}} = 0$. First, if a_x and a_{xx} take nonzero values while the other coefficients vanish, the inferred equation corresponds to the advection-diffusion equation. In this case, a_x and a_{xx} represent the flow velocity and the diffusion coefficient, respectively. In this system, the initial structure is advected while gradually diffusing. If a_x and a_{xxx} vanish, the inferred equation reduces to the Burgers equation. In this case, a_{nx} represents the nonlinearity and a_{xx} represents the dissipation, which sustain a shock-wave structure. If a_x and a_{xx} vanish, the governing equation reduces to the KdV equation. Here, a_{xxx} represents the dispersive effect, which sustains a solitary-wave structure through its balance with the nonlinearity. The Burgers equation and the KdV equation can also appear simultaneously, in which case the inferred equation corresponds to the KdV-Burgers equation.

III. BENCHMARK TESTS OF PINNS

In this section, we demonstrate that PINNs can successfully infer both the structure of the governing PDE and its coefficients from solution data. First, we present results for the advection-diffusion, Burgers, and KdV equations. We then examine parameter scans over several PDE coefficients. Finally, we show results for the composite KdV-Burgers equation.

A. Method of benchmark tests

Validation datasets are generated using the Runge-Kutta method implemented in the SciPy package [30]. We compute one-dimensional solutions of the advection-diffusion, Burgers, KdV, and KdV-Burgers equations, all starting from a common Gaussian initial condition as

$$n_0(x) = \exp\left[-\frac{(x-5.0)^2}{4.0}\right]. \tag{21}$$

The system length is $L_x = 10.0$, which is discretized into $n_x = 100$ mesh points. We time integrate the equations up to $t = 8.0$ using $n_t = 100$ time steps; i.e., the time step is $\Delta t = 0.08$. Periodic boundary conditions are applied at $x = 0$ and $x = L_x$. The entire domain, $0 \leqslant x \leqslant 10.0$ and $0 \leqslant t \leqslant 8.0$, is used for training. The PINN model consists of 9 dense layers with 20 neurons each, using hyperbolic tangent activation in the hidden layers and a linear activation in the output layer. The Adam optimizer with a learning rate of 0.001 is applied. The model is trained for 10 000 epochs, and the batch size is 256. The loss weight for the equation term, k_{eq}, is set to 100, which is sufficiently large to ensure learning of the governing equation. We note that $k_{\mathrm{eq}} \sim 1$ can also be acceptable in some simple benchmark settings.

B. Result of typical equations: advection-diffusion, Burgers, and KdV equations

First, we infer the coefficients of the (1) advection-diffusion, (2) Burgers, and (3) KdV equations from their solution data as benchmark tests. Figure 1 shows the best-fitting cases for each equation: (1) $a_x = 1.0$ and $a_{xx} = -0.2$; (2) $a_{xx} = -0.2$ and $a_{nx} = 1.0$; and (3) $a_{xxx} = 0.1$ and

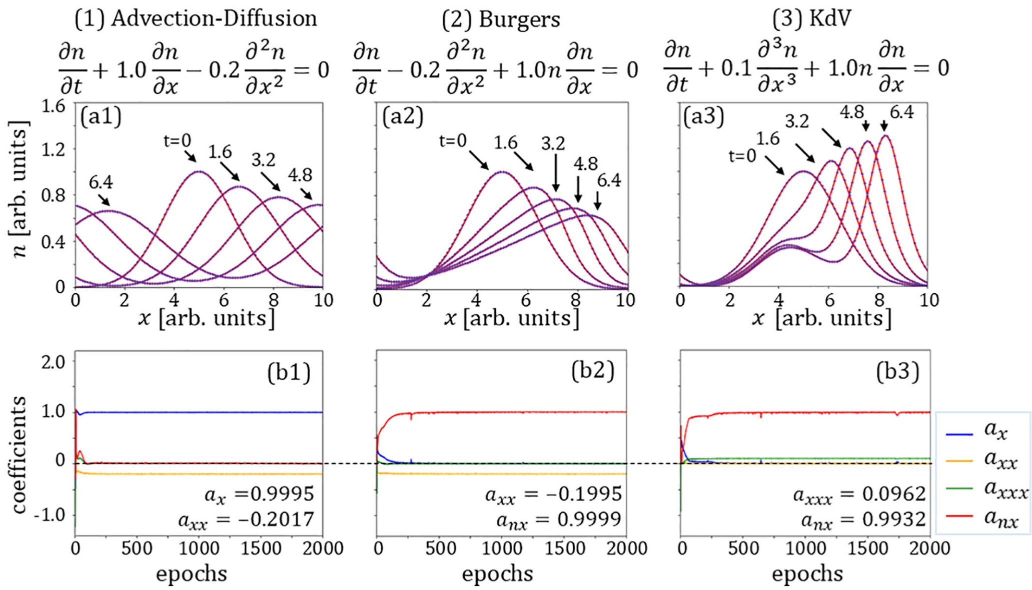

FIG. 1. Overview of the benchmark tests for the (1) advection-diffusion, (2) Burgers, and (3) KdV equations. Panels (a1)–(a3) show the comparison between the training data (red solid line) and the predicted data (blue dotted line). Panels (b1)–(b3) show the learning process of the coefficients (a_x: blue, a_{xx}: yellow, a_{xxx}: green, a_{nx}: red). The values of inferred coefficients after 2000 epochs are also shown in each panel.

$a_{nx} = 1.0$. Figures 1(a1)–1(a3) illustrate the differences between the training and predicted data, while Figs. 1(b1)–1(b3) show the learning process of coefficients and their value after 2000 epochs.

In the case of the advection-diffusion equation [Fig. 1(a1)], the initial Gaussian profile is advected with a velocity $v_x = 1$ and gradually damped by diffusion. In the case of the Burgers equation [Fig. 1(a2)], the initial Gaussian steepens due to nonlinear advection. The dissipation then balances the steepening, leading to the formation of a shock wave. In the case of the KdV equation [Fig. 1(a3)], the initial Gaussian also steepens, as in the case of the Burgers equation, and subsequently develops into a solitary wave. Here, the dispersive effect balances the steepening, resulting in the formation of a solitary wave.

Next, we examine the convergence of the inferred coefficients shown in Figs. 1(b1)–1(b3). In all cases, the coefficients converge in the early stage of training. In the advection-diffusion case, the coefficients converge within approximately 100 epochs. In the Burgers and KdV cases, which have the nonlinear terms, the training requires more epochs; nevertheless, the coefficients converge within roughly 500 epochs.

We then evaluate the errors in the inferred coefficients. Figure 2 displays the mean errors of the inferred coefficients. The mean error is computed as the average relative error $|(a_s^{\mathrm{PINN}} - a_s^{\mathrm{true}})/a_s^{\mathrm{true}}|$, where a_s^{PINN} and a_s^{true} denote the inferred and true values of the coefficient, respectively, and s denotes x, xx, xxx, or nx. In the training data for the advection-diffusion equation [Fig. 2(a)], the coefficients are predicted with errors below 0.3% in all cases examined. This result indicates that the PINN performs well for the advection-diffusion equation, i.e., a simple linear PDE. In the case of the Burgers equation [Fig. 2(b)], which contains a nonlinear term, the PINN still succeeds in almost all parameter regimes. However, as the nonlinear term a_{nx} becomes larger relative to the dissipative term a_{xx}, the prediction error increases. In particular, the error exceeds 1% for the parameter set $(a_{xx}, a_{nx}) = (-0.1, 2.0)$, which corresponds to the case with the strongest nonlinearity. In the case of the KdV equation [Fig. 2(c)], when the dispersion term is large ($a_{xxx} = 0.1$) and the nonlinearity is weak ($a_{nx} = 1.0$), the prediction error remains below 1%. However, when the nonlinearity becomes

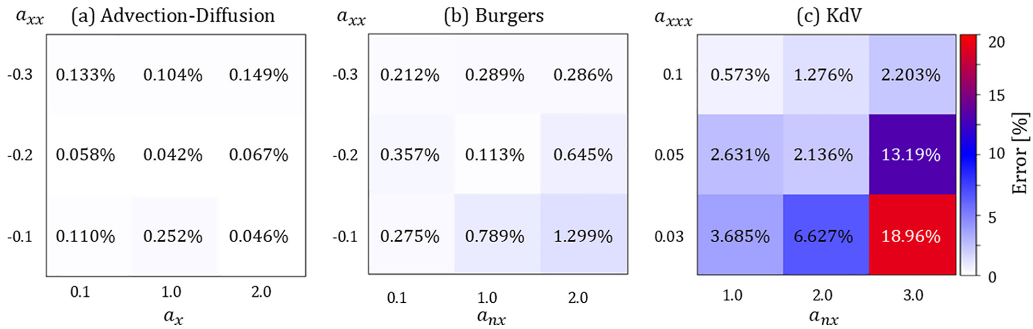

FIG. 2. Mean error heatmap of the inferred coefficients for the cases of (a) advection-diffusion, (b) Burgers, and (c) KdV equations.

strong ($a_{nx} \geqslant 2.0$), the error exceeds 1%. Even when the nonlinearity is weak ($a_{nx} = 1.0$), the error also exceeds 1% if the dispersion is weak ($a_{xxx} \leqslant 0.05$). Additionally, in cases with strong nonlinearity ($a_{nx} = 3.0$) and weak dispersion ($a_{xxx} \leqslant 0.05$), the error becomes larger than 10%. These large errors can be attributed to the breakup of the initial Gaussian profile into multiple sharp solitary waves. In strongly nonlinear cases, the solitary waves generated after the breakup become narrower and steeper. Accurately resolving such sharp structures requires a large number of data points, which leads to larger prediction errors.

C. Result of composite KdV-Burgers equation

Here, we consider the case of the KdV-Burgers equation, which is a composite system combining the Burgers and KdV equations. Figure 3 shows the evolution of (a) L_{data} and $k_{\mathrm{eq}}L_{\mathrm{eq}}$, and (b) the coefficients a_x, a_{xx}, a_{xxx}, and a_{nx} during the learning process. Snapshots of the training and predicted data are shown in Fig. 3(c). The parameter set $(a_{xx}, a_{xxx}, a_{nx}) = (-0.2, 0.1, 1.0)$ is used in Figs. 3(a)–3(c). Figure 3(d) shows the mean error heatmap of the inferred a_{xx} and a_{xxx} obtained through the parameter scan, where a_{xx} and a_{xxx} are scanned while a_{nx} is fixed at 1.0.

In the composite case, the loss decreases steadily during the learning process [Fig. 3(a)]. Both L_{data} and $k_{\mathrm{eq}}L_{\mathrm{eq}}$ fall below 10^{-6}. The coefficients are also accurately estimated [Fig. 3(b)]. The solution exhibits a composite structure consisting of a shock and a solitary wave [Fig. 3(c)], indicating that the neural network can accurately reconstruct the training data. Through a parameter scan over a_{xxx} and a_{nx}, the error remains below 2%. For instance, the error for the parameter set $(a_{xx}, a_{xxx}, a_{nx}) = (-0.05, 0.03, 1.0)$ stays at 1.788% [lower-left region of Fig. 3(d)], in contrast to the KdV case with $(a_{xxx}, a_{nx}) = (0.03, 1.0)$, where the error is 3.685% [Fig. 2(c)]. This indicates that the dissipative term relaxes the profile and consequently makes the estimation easier.

IV. VALIDATION OF SOLITARY WAVES DRIVEN BY PULSE LASER

In this section, we present the simulation results of a one-dimensional particle simulation and the application of the PINN to this data. After presenting the numerical method, we describe the process through which solitary waves emerge in the simulation. Then, we show that the PINN successfully reconstructs the original simulation data and infers coefficients that are consistent with theoretical predictions.

A. Numerical method of particle simulation

The original simulation data are computed using the electromagnetic relativistic particle simulation code EPIC3D [31]. The simulation domain is $L_x \times L_y = 0.04\ \mu\mathrm{m} \times 10.0\ \mu\mathrm{m}$, divided into 4×1000 meshes, giving a mesh size of $0.01\ \mu\mathrm{m}$. The target plasma consists of fully ionized,

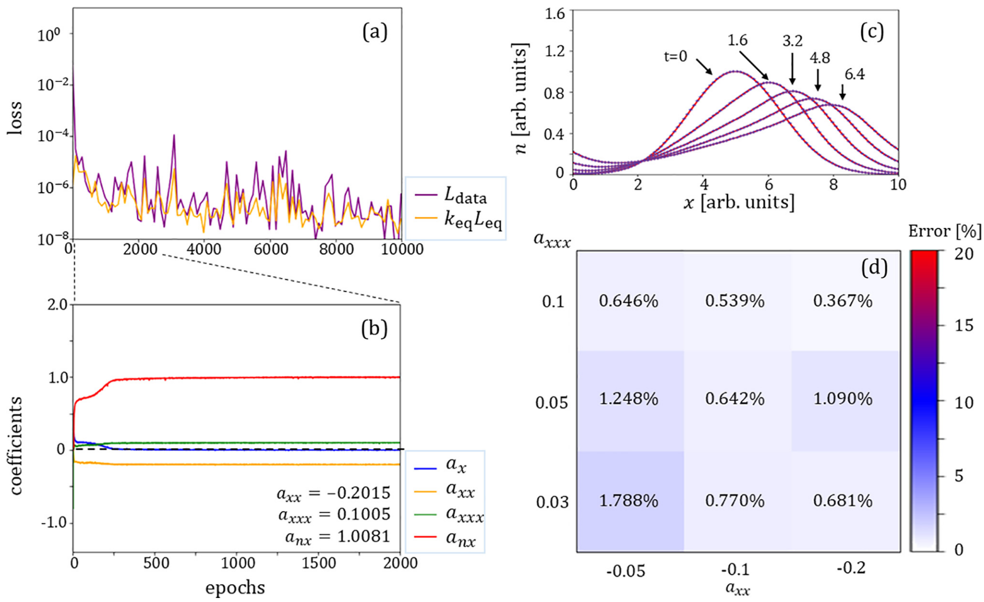

FIG. 3. The evolution of (a) L_{data} (purple) and $k_{\text{eq}}L_{\text{eq}}$ (yellow); (b) the coefficients a_x (blue), a_{xx} (yellow), a_{xxx} (green), and a_{nx} (red) during the learning process; (c) snapshots of the training data (red solid line) and predicted data (blue dotted line); and (d) the mean error heatmap of inferred a_{xx} and a_{xxx} obtained through the parameter scan over a_{xx} and a_{xxx}. Here, the parameter set $(a_{xx}, a_{xxx}, a_{nx}) = (-0.2, 0.1, 1.0)$ is used in Figs. 3(a)–3(c). a_{nx} is fixed at 1.0 in Fig. 3(d).

collisionless carbon (C^{6+}) with an electron density of $n_e = 50n_c$, where $n_c = 1.70 \times 10^{21}\ \text{cm}^{-3}$ is the cutoff density for the injected laser wavelength $\lambda_L = 0.810\ \mu\text{m}$. The plasma initially occupies the region $4.0\ \mu\text{m} \leqslant y \leqslant 6.0\ \mu\text{m}$. The number of PIC particles for ions is 20 per mesh. The laser pulse is linearly polarized in the x direction. The laser is injected from an antenna located at $y = 0.04\ \mu\text{m}$. It begins to propagate in the y direction at $t = 0$ fs and reaches peak at $t = 200$ fs. The pulse width is $\tau_0 = 83$ fs, defined as the full width at half maximum. The peak laser intensity is $I = 2.00 \times 10^{20}\ \text{W/cm}^2$, corresponding to $a_0 = 9.79$, where a_0 is the normalized laser amplitude defined as $a_0 \equiv eE_0/(m_e c\omega_L)$. Here, m_e denotes the electron mass, c denotes the speed of light, and ω_L and E_0 denote the laser frequency and peak electric field, respectively. The boundary conditions for both fields and particles are periodic in the x and z directions. For the y direction, the boundary conditions for the fields are the Mur absorbing boundary condition for the Maxwell equations, formulated as

$$\left(\frac{\partial}{\partial y} + \frac{1}{c}\frac{\partial}{\partial t}\right)\boldsymbol{E}_t = 0, \quad \left(\frac{\partial}{\partial y} + \frac{1}{c}\frac{\partial}{\partial t}\right)\boldsymbol{B}_t = 0 \tag{22}$$

at $y = 0, L_y$, where $\boldsymbol{E}_t$ and $\boldsymbol{B}_t$ represent the field components perpendicular to the y direction. For particles, the boundary conditions are transparent: particles that reach the boundary are fixed there and their charge is set to zero.

B. Physics of solitary wave driven by pulse laser

Here, we describe the process of solitary-wave formation driven by the laser pulse. Figure 4(a) shows the temporal evolution of the cross-sectional ion density. Figure 4(b) presents cross-sectional profiles of the ion density n_i, electron density n_e, and electric field E_y at $t = 233,\ 267$, and 300 fs. At first, the laser pulse pushes the electrons via the ponderomotive force, while the ions are not directly

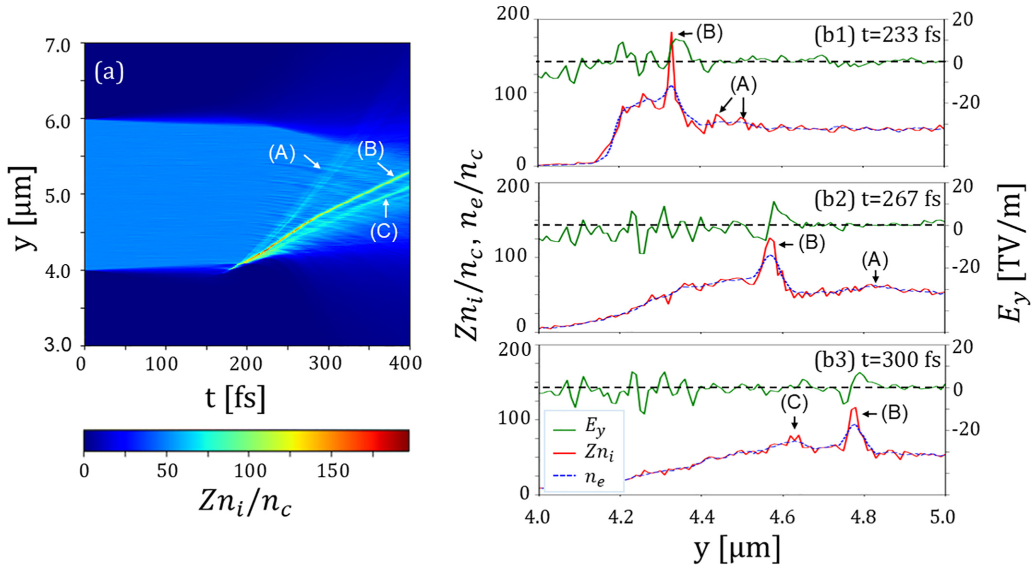

FIG. 4. Results of the particle simulation for laser-driven solitary waves. (a) Temporal evolution of the cross-sectional ion density. (b) Cross-sectional profiles of the ion density n_i (red solid line), electric field E_y (green solid line), and electron density n_e (blue dotted line) at $t = 233,\ 267$, and 300 fs. The black dashed line indicates $E_y = 0$.

accelerated on the femtosecond timescale. As a result, charge separation between the displaced electrons and the background ions generates a strong electric field E_y, which accelerates the ions. The accelerated ions form a pronounced density peak up to $t \simeq 180$ fs. After that, the peak structure propagates along the y direction and breaks up into three distinguishable parts. The fastest solitary wave [(A) in Figs. 4(a) and 4(b1)] propagates in the y direction with an almost constant velocity of $v_{sA} = 0.0369c$. This wave initially has a small amplitude and breaks into several smaller waves. It eventually disappears due to a collision with the rarefaction wave from the rear surface at $t \simeq 340$ fs. The main solitary wave [(B) in Figs. 4(a) and 4(b1)–4(b3)] is sustained by a strong electric field E_y and propagates in the y direction with a trailing thermalized region. Only the main solitary wave is clearly visible between $t = 200$ and 267 fs. In this time interval, its velocity remains nearly constant at $v_{sB} = 0.0196c$. The secondary solitary wave [(C) in Figs. 4(a) and 4(b3)] emerges from the thermalized region generated by the main solitary wave. It propagates while trailing the main solitary wave with a velocity of $v_{sC} = 0.0206\,c$, which is almost the same as that of the main solitary wave.

C. Inferring of the governing equation by PINN

To clarify the characteristics of the main solitary wave, we apply the PINN model to the original simulation data shown in Sec. IV B. We use a neural network with the same architecture as in Sec. III. Because the breakup of the solitary wave complicates the PINN prediction, as shown in Sec. III B, we focus on the region where the main solitary wave exhibits its characteristics most clearly: $(x_{\min}, x_{\max}) = (4.00\ \mu\text{m}, 4.75\ \mu\text{m})$ and $(t_{\min}, t_{\max}) = (200\ \text{fs}, 267\ \text{fs})$. The weight of the loss function is set to $k_{\text{eq}} = 10^{-2}$, which is smaller than that in the benchmark tests in Sec. III. This is because the original simulation data do not strictly satisfy a specific partial differential equation. A smaller value of k_{eq} is therefore chosen to enable robust inference of the governing equation from such data.

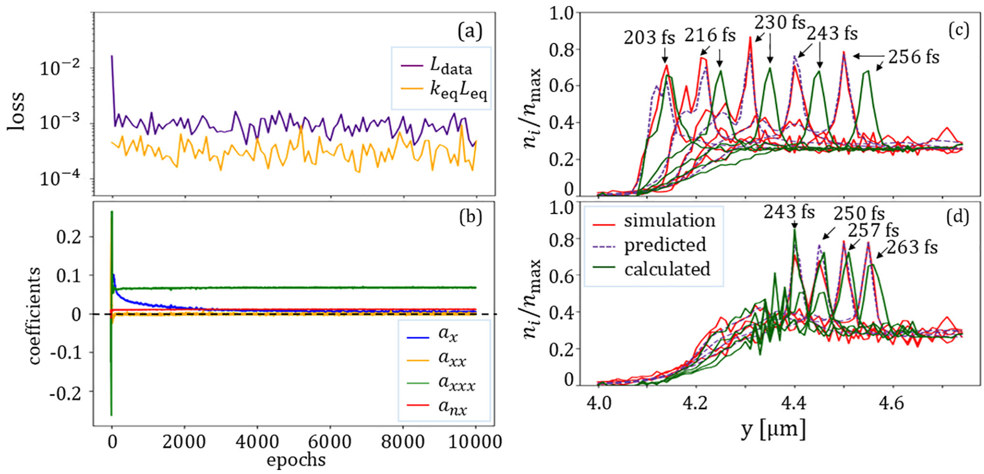

FIG. 5. The evolution of (a) L_{data} (purple) and $k_{\mathrm{eq}}L_{\mathrm{eq}}$ (yellow), and (b) the coefficients a_x (blue), a_{xx} (yellow), a_{xxx} (green), and a_{nx} (red) during the learning process. (c), (d) Cross-sectional profiles of the original simulation data (red solid line), PINN-predicted data (blue dashed line), and the solution of the equation with the PINN-inferred coefficients (green solid line). The profiles of the original simulation data at (c) 200 fs and (d) 237 fs are used as the initial conditions to compute the solution of the equation with the PINN-inferred coefficients.

We present the results of the PINN training in Fig. 5 and Table I. Figure 5(a) shows the evolution of the PINN loss functions L_{data} and $k_{\mathrm{eq}}L_{\mathrm{eq}}$ during the learning process. The residual term L_{data} decreases monotonically, indicating that the PINN properly learns the original simulation data. The value of L_{data} is larger than that in the benchmark tests because the original simulation data do not strictly satisfy the inferred governing equation and no converged solution exists that simultaneously yields $L_{\mathrm{data}} = 0$ and $L_{\mathrm{eq}} = 0$. On the other hand, the value of $k_{\mathrm{eq}}L_{\mathrm{eq}}$ is sufficiently small to conclude that the coefficients have been properly inferred. The ratio between L_{data} and $k_{\mathrm{eq}}L_{\mathrm{eq}}$ is below 10^1, which is consistent with those reported in previous studies [32–34]. Figure 5(b) shows the evolution of the coefficients in the term L_{eq} during the learning process. The PINN-inferred coefficients and the theoretical values from Eq. (13) are summarized in Table I. To calculate the theoretical values, the mean background electron temperature $T_e \simeq 33$ keV is obtained by averaging the spatial distribution of the electron energy over the region traversed by the solitary wave. This temperature does not necessarily match the temperature defined from the slope of the logarithm of a Maxwellian distribution function, because the present system is intrinsically nonthermal. Nevertheless, the inferred coefficients converge within the first 5000 epochs, and the converged values of a_{xxx} and a_{nx} are of the same order as the theoretical predictions, indicating that the KdV equation governs this system. The remaining discrepancy between the PINN-inferred coefficients and the theoretical value can be attributed primarily to the difference in the temperature definition. In particular, the dispersion coefficient $a_{xxx} = (1/2)c_s\lambda_{\mathrm{De}}^2$ scales as $T_e^{3/2}$, whereas the nonlinear coefficient $a_{nx} = Zc_s/n_0$ scales

TABLE I. Inferred coefficients by the PINN and theory.

Coefficients	PINN (sim. units)	PINN (CGS units)	Theory
a_x	0.004 20		
a_{xx}	0.000 20		
a_{xxx}	0.067 41	10.1×10^{-5} cm^3/s	1.35×10^{-5} cm^3/s
a_{nx}	0.010 51	5.58×10^{-15} cm^4/s	8.88×10^{-15} cm^4/s

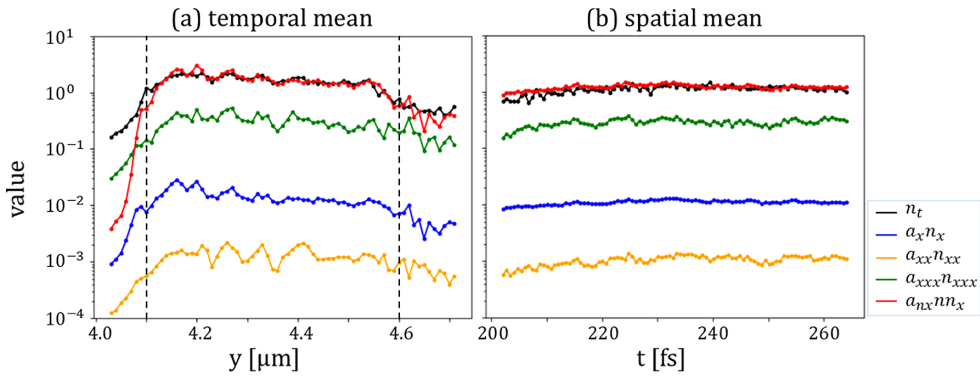

FIG. 6. (a) Temporal mean profile of each differential term, i.e., advection $a_x n_x$ (blue), dissipation $a_{xx} n_{xx}$ (yellow), dispersion $a_{xxx} n_{xxx}$ (green), nonlinearity $a_{nx} n_{nx}$ (red), and the time derivative of density n_t (black). The temporal mean is calculated over the interval 200 fs $\leqslant t \leqslant$ 267 fs. The black dashed line indicates the position where the main solitary wave exists at the initial and the last snapshot. (b) Temporal evolution of the spatial mean of each differential term corresponding to those shown in Fig. 6(a). The spatial mean is calculated over the region 4.0 μm $\leqslant y \leqslant$ 4.75 μm.

as $T_e^{1/2}$. Therefore, the dispersion term is more sensitive to uncertainty in the electron temperature, which explains its larger deviation from the theoretical estimate. We also confirmed through a parameter scan using five different random seeds for PINN initialization that the coefficients of the same order are consistently reproduced.

To verify the PINN-predicted data and inferred coefficients, we compare three types of data in Figs. 5(c) and 5(d): the original simulation data (simulation), the PINN-predicted data (predicted), and the solution of the equation with the PINN-inferred coefficients (calculated). The calculated solution is obtained using the same code as in Sec. III. The boundary conditions are a fixed boundary at $y = 4.0$ μm and a transparent boundary at $y = 4.75$ μm, both implemented with a Krook operator. In the interval 200 fs $< t <$ 237 fs, a secondary solitary wave separates from the main solitary wave in the simulation data. To investigate the influence of this transient splitting, we compute two numerical solutions using different initial conditions at (c) $t = 200$ fs, which includes the onset of the splitting, and (d) $t = 237$ fs, after the splitting has subsided. For both initial conditions, the PINN-predicted data (blue dashed lines) agree well with the original simulation data, indicating that the neural network successfully reconstructs the training data. In contrast, the calculated solution starting from $t = 200$ fs shows a solitary wave slightly ahead of that in the original simulation data [Fig. 5(c)], because the inferred equation does not explicitly capture the splitting event present in the early data. However, the spatial deviation between simulation data and numerical solution remains constant after $t = 216$ fs, supporting a reasonable level of consistency. When the numerical solution is initialized at $t = 237$ fs, however, the solitary-wave position aligns closely with the simulation data [Fig. 5(d)]. These results indicate that the PINN-inferred coefficients accurately describe the stable solitary-wave propagation once the transient splitting is excluded.

Finally, the temporal and spatial means of each differential term are evaluated in Fig. 6. Figure 6(a) shows the temporal mean at each spatial point. The temporal mean is calculated over the interval 200 fs $\leqslant t \leqslant$ 267 fs. The dispersion term $a_{xxx} n_{xxx}$ and the nonlinear term $a_{nx} n_{nx}$ remain nearly constant in the region traversed by the main solitary wave. Here, $y = 4.1$ μm corresponds to the position where the peak structure first emerges, while $y = 4.6$ μm corresponds to the position where the main solitary wave disappears from the region used for training. The advection term $a_x n_x$ and the dissipation term $a_{xx} n_{xx}$ remain below 1% of the time derivative of density n_t, indicating that advection and dissipation terms are negligible to describe the governing partial differential equation. This result implies that a nonlinear KdV-like equation is inferred as the governing equation. Figure 6(b) shows the temporal evolution of the spatial mean at each time step. The spatial mean is calculated over the region 4.0 μm $\leqslant y \leqslant$ 4.75 μm. The spatial mean also exhibits the same relative magnitudes among the differential terms. All differential terms maintain nearly constant values over the time interval used for the PINN analysis, indicating that the form of the governing equation remains unchanged throughout this period.

We also assessed the uncertainty of the inferred model by varying the network architecture and the fraction of training data. We confirmed that this result is robust with respect to variations in the number of layers; increasing or decreasing the number of layers by 2 does not change the inferred equation. Regarding the fraction of training data, the inferred model gradually approaches a simpler advection-type equation as the data fraction is reduced. This tendency indicates that sufficient data are required to distinguish the steady propagation of a solitary wave from the pure advective propagation of a single peak structure, as discussed in the benchmark test.

V. CONCLUSION

We have introduced a PINN-based method to infer the structure of the governing partial differential equations that describe solitary waves in one-dimensional PIC simulation data. We have demonstrated that the PINN is capable not only of reconstructing the original simulation data but also of inferring the governing equation that describes the system. The mean values of the differential terms suggest that a nonlinear KdV-like equation is inferred as the governing equation. Our results provide quantitative evidence that laser-driven solitary waves are described by KdV-type solitons, which is essential for understanding various nonlinear wave phenomena inherent to plasmas.

In this study, we use only the ion density to identify the solitary-wave structure. However, theory predicts that the ion flow velocity and electrostatic potential are also important for capturing solitary-wave behavior. Extending the present PINN analysis to these quantities is an important direction for future work.

ACKNOWLEDGMENTS

The authors would like to thank Dr. Yasuaki Kishimoto in Kyoto University for his valuable comments on this study. This work was supported by JSPS KAKENHI Grants No. 21H04452, No. 22K14019, No. 23K20038, and No. 24K06992. In this research work, we used the supercomputer of ACCMS, Kyoto University.

DATA AVAILABILITY

The data that support the findings of this article are not publicly available upon publication because it is not technically feasible and/or the cost of preparing, depositing, and hosting the data would be prohibitive within the terms of this research project. The data are available from the authors upon reasonable request.

[1] I. B. Bernstein, J. M. Greene, and M. D. Kruskal, Exact nonlinear plasma oscillations, Phys. Rev. **108**, 546 (1957).

[2] R. E. Ergun, C. W. Carlson, J. P. McFadden, F. S. Mozer, L. Muschietti, I. Roth, and R. J. Strangeway, Debye-scale plasma structures associated with magnetic-field-aligned electric fields, Phys. Rev. Lett. **81**, 826 (1998).

[3] C. A. Cattell, J. Crumley, J. Dombeck, J. R. Wygant, and F. S. Mozer, Polar observations of solitary waves at the Earth's magnetopause, Geophys. Res. Lett. **29**, 9 (2002).

[4] H. Matsumoto, L. A. Frank, Y. Omura, H. Kojima, W. R. Paterson, M. Tsutsui, R. R. Anderson, S. Horiyama, S. Kokubun, and T. Yamamoto, Generation mechanism of ESW based on Geotail plasma wave observation, plasma observation and particle simulation, Geophys. Res. Lett. **26**, 421 (1999).

[5] G. S. Lakhina, S. V. Singh, R. Rubia, and T. Sreeraj, A review of nonlinear fluid models for ion-and electron-acoustic solitons and double layers: Application to weak double layers and electrostatic solitary waves in the solar wind and the lunar wake, Phys. Plasmas **25**, 080501 (2018).

[6] J. D. Williams, L.-J. Chen, W. S. Kurth, D. A. Gurnett, and M. K. Dougherty, Electrostatic solitary structures observed at Saturn, Geophys. Res. Lett. **33**, 61103 (2006).

[7] L. Z. Hadid *et al.*, Solar Orbiter's first Venus flyby: Observations from the radio and plasma wave instrument, Astron. Astrophys. **656**, A18 (2021).

[8] R. Rubia, S. V. Singh, G. S. Lakhina, S. Devanandhan, M. B. Dhanya, and T. Kamalam, Electrostatic solitary waves in the Venusian ionosphere pervaded by the solar wind: A theoretical perspective, Astrophys. J. **950**, 111 (2023).

[9] M. S. Afify, I. S. Elkamash, M. Shihab, and W. M. Moslem, Evolution of ion-acoustic soliton waves in Venus's ionosphere permeated by the solar wind, Adv. Space Res. **67**, 4110 (2021).

[10] K. Singh, A. Kakad, B. Kakad, and N. S. Saini, Evolution of ion acoustic solitary waves in pulsar wind, Mon. Not. R. Astron. Soc. **500**, 1612 (2020).

[11] W. L. Zhang, B. Qiao, T. W. Huang, X. F. Shen, W. Y. You, X. Q. Yan, S. Z. Wu, C. T. Zhou, and X. T. He, Quasi-monoenergetic ion beam acceleration by laser-driven shock and solitary waves in near-critical plasmas, Phys. Plasmas **23**, 073118 (2016).

[12] A. Macchi, A. S. Nindrayog, and F. Pegoraro, Solitary versus shock wave acceleration in laser-plasma interactions, Phys. Rev. E **85**, 046402 (2012).

[13] A. Zhidkov, M. Uesaka, A. Sasaki, and H. Daido, Ion acceleration in a solitary wave by an intense picosecond laser pulse, Phys. Rev. Lett. **89**, 215002 (2002).

[14] R. Matsui, Y. Fukuda, and Y. Kishimoto, Dynamics of the boundary layer created by the explosion of a dense object in an ambient dilute gas triggered by a high power laser, Phys. Rev. E **100**, 013203 (2019).

[15] D. J. Korteweg and G. de Vries, XLI. On the change of form of long waves advancing in a rectangular canal, and on a new type of long stationary waves, London Edinburgh Dublin Philos. Mag. J. Sci. **39**, 422 (1895).

[16] N. J. Zabusky and M. D. Kruskal, Interaction of "solitons" in a collisionless plasma and the recurrence of initial states, Phys. Rev. Lett. **15**, 240 (1965).

[17] C. S. Gardner and G. K. Morikawa, *Similarity in the Asymptotic Behavior of Collision-Free Hydromagnetic Waves and Water Waves* (Courant Institute of Mathematical Sciences, New York, 1960).

[18] H. Washimi and T. Taniuti, Propagation of ion-acoustic solitary waves of small amplitude, Phys. Rev. Lett. **17**, 996 (1966).

[19] R. Hirota, Exact solution of the Korteweg–de Vries equation for multiple collisions of solitons, Phys. Rev. Lett. **27**, 1192 (1971).

[20] R. M. Miura, C. S. Gardner, and M. D. Kruskal, Korteweg–de Vries equation and generalizations. II. Existence of conservation laws and constants of motion, J. Math. Phys. **9**, 1204 (1968).

[21] S. S. Ghosh and G. S. Lakhina, Anomalous width variation of rarefactive ion acoustic solitary waves in the context of auroral plasmas, Nonlinear Processes Geophys. **11**, 219 (2004).

[22] M. Shamir, T. Arshad, I. A. Khan, and K. Malakit, Electrostatic solitary waves in the Earth's magnetosheath: An analytical approach, Phys. Fluids **37**, 026121 (2025).

[23] C. Meng, S. Griesemer, D. Cao, S. Seo, and Y. Liu, When physics meets machine learning: A survey of physics-informed machine learning, Mach. Learn. Comput. Sci. Eng. **1**, 20 (2025).

[24] M. Raissi, P. Perdikaris, and G. E. Karniadakis, Physics-informed neural networks: A deep learning framework for solving forward and inverse problems involving nonlinear partial differential equations, J. Comput. Phys. **378**, 686 (2019).

[25] Z. Ren, S. Zhou, D. Liu, and Q. Liu, Physics-informed neural networks: A review of methodological evolution, theoretical foundations, and interdisciplinary frontiers toward next-generation scientific computing, Appl. Sci. **15**, 8092 (2025).

[26] M. Kang, H. Li, Q. Tan, Z. Wang, R. Li, J. Zhao, H. Xiang, and D. Fan, Physics-informed neural networks for the Korteweg-de Vries equation for internal solitary wave problem: Forward simulation and inverse parameter estimation, Phys. Fluids **37**, 073615 (2025).

[27] J. Guo, Z. Liu, and C. Hou, Error estimates for a physics-informed neural network in solving KdV equations, Mach. Learn. **7**, 015026 (2026).

[28] Y.-J. Wang, W.-B. Xu, B. Wang, and D.-X. Xu, Conservation-laws-informed physics-informed neural networks for solving the KdV equation, Physica D **494**, 135256 (2026).

[29] C. R. Jisha, K. J. Prakash, T. K. Riyasudheen, and S. Sahadevan, Physics-informed neural networks with energy constraints for coupled KdV equations: Analytical and computational insights into soliton interactions, Eur. Phys. J. Plus **141**, 98 (2026).

[30] P. Virtanen *et al.*, SciPy 1.0: Fundamental algorithms for scientific computing in Python, Nat. Methods **17**, 261 (2020).

[31] Y. Kishimoto and T. Masaki, A paradigm of kinetic simulation including atomic and relaxation processes: A sudden event in a lightning process, J. Plasma Phys. **72**, 971 (2006).

[32] M. Berardi, F. V. Difonzo, and M. Icardi, Inverse physics-informed neural networks for transport models in porous materials, Comput. Methods Appl. Mech. Eng. **435**, 117628 (2025).

[33] M. Yin, X. Zheng, J. D. Humphrey, and G. E. Karniadakis, Non-invasive inference of thrombus material properties with physics-informed neural networks, Comput. Methods Appl. Mech. Eng. **375**, 113603 (2021).

[34] C. Zhou, J. Chen, Z. Yang, and C. E. Png, Dual-balancing for physics-informed neural networks, in *Proceedings of the 34th International Joint Conference on Artificial Intelligence* (International Joint Conferences on Artificial Intelligence Organization, Montreal, Canada and Guangzhou, China, 2025), pp. 7164–7172.